CHAPTER II

FUNDAMENTAL KNOWLEDGE AND LITERATURE REVIEW

2.1 Carbon nanotubes (CNTs)

2.1.1 Structure of CNTs

Carbon nanotubes (CNTs) which were discovered in 1991 (Iijima, 1991) are allotropes of carbon with a cylindrical structure, built from sp^2 carbon units and consist of honeycomb lattices known as graphene sheet. They are a seamless structure with a diameter of a few nanometers but lengths of many microns.

They can be classified into 2 main types: single-walled carbon nanotubes (SWCNTs) and multi-walled carbon nanotubes (MWCNTs). The SWCNTs are made of a single rolled graphite sheet with a typical diameter of about 1 nm while the MWCNTs are closed graphite tubules rolled like a graphite sheet with the distance between sheets about 0.34 nm as shown in Figure 2.1 (a) and (b), respectively.

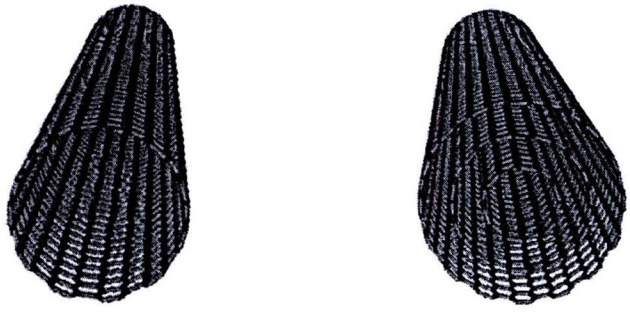

(a) (b)

Figure 2.1 Structures of (a) SWCNTs and (b) MWCNTs.
(itech.dickinson.edu)

Depending on how the graphene sheets of a nanotube are rolled together at different chirality and angle (Saito et al., 1998), they are classified by their chiral vectors (C_h) as shown in equation 2.1 into armchair, zigzag and chiral shapes as shown in Figure 2.2.

$$C_h = na_1 + ma_2 \equiv (n, m) \qquad (2.1)$$

where a_1 and a_2 are unit vectors in the two-dimensional hexagonal lattice

n and m are integers

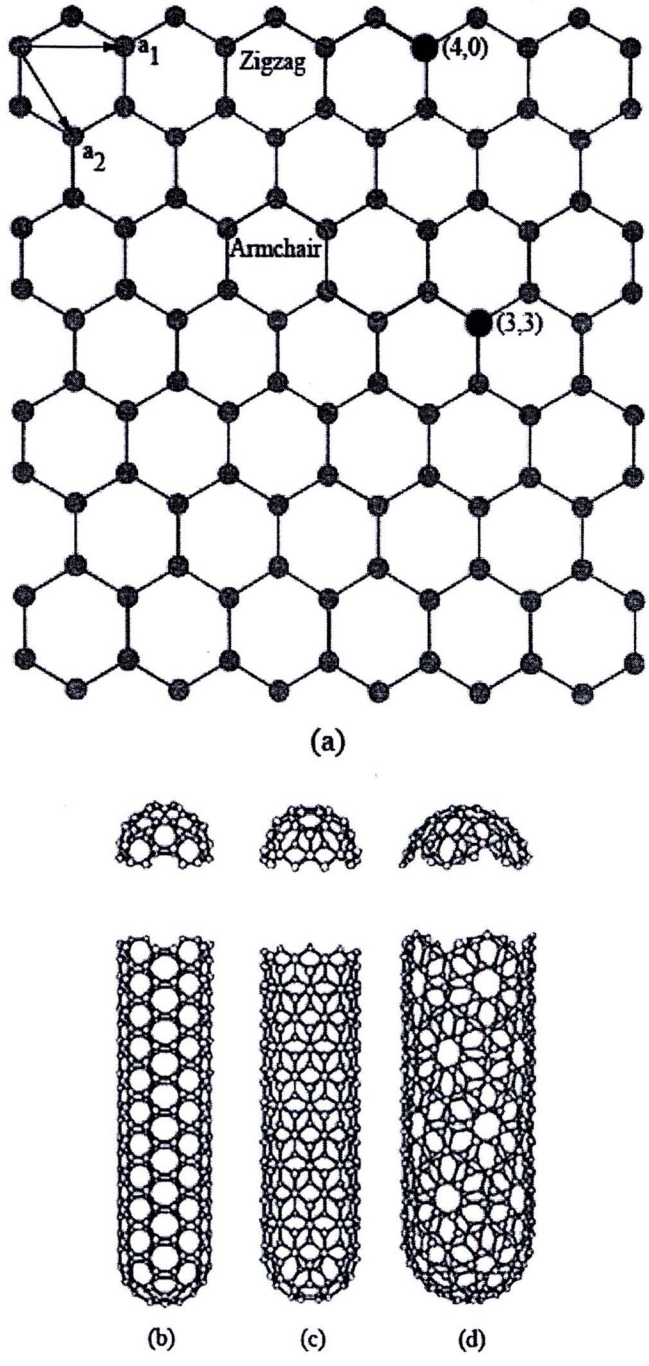

Figure 2.2 Structures of (a) an unrolled graphene sheet of a nanotube, (b) an armchair nanotube, (c) a zigzag nanotube and (d) a chiral nanotube

(cnx.org/content/m22580/latest/)

Another important parameter which determines properties of nanotube along with diameter of the tube is chiral angle (θ), the angle between C_h and a_1 with value in the range of 0° and 30°. An armchair nanotube corresponds to the case of n = m, that is C_h = (n, n) with the chiral angle of 30°, while a zigzag nanotube corresponds to the case of m = 0, or C_h = (n, 0) with the chiral angle of 0°. All other (n, m) chiral vectors correspond to chiral nanotubes with the chiral angles between 0° and 30° as shown in Table 2.1

Table 2.1 Classification of carbon nanotubes and their electrical conductivity

Type	Chiral vector (C_h)	Chiral angle (θ)	Electrical conductivity
Armchair	(n,n)	30°	Metallic
Zigzag	(n,0)	0°	Metallic or Semiconducting*
Chiral	(n,m)	0°-30°	Metallic or Semiconducting*

*Electrical conductivity of zigzag and chiral nanotubes depend on theirs chiral vector

The characteristic structure of a nanotube strongly affects its electrical properties which the armchair nanotubes are always metallic, while zigzag and chiral nanotubes are either metallic or semiconducting, depending on theirs chiral vector.

2.1.2 Physical properties of CNTs

The CNTs are known to have remarkable electronic and mechanical properties because of their unique structures, leading to application in nano-electronic and nano-mechanical devices, respectively. Furthermore, properties of carbon nanotubes can also be expanded to thermal and optical properties as well.

As a result of the carbon–carbon sp^2 bonding, they are predicted to have high stiffness and axial strength which must ultimately depend on the strength of its interatomic bonds (Paradise and Goswami, 2007)). On a per-bond basis, the graphitic sp^2 bonding is 33% stronger than the sp^3 bonding of diamond, the hardest substance in nature. Experimental and theoretical results have shown an elastic modulus of greater than 1 TPa (the elastic modulus of diamond is 1.2 TPa) and reported strengths 10–100 times higher than the strongest steel at a fraction of the weight (Thostenson, Ren, and Chou, 2001). Experimental result in tensile strengths

has shown in the range from 11 to 63 GPa, with dependence on the outer shell diameter, which is not far from the theoretical yield strength of about 100 GPa. From Table 2.2, the CNTs show their theoretical tensile strength over diamond. This is particularly beneficial for high-strength properties of composites based on nanotubes.

Table 2.2 Theoretical mechanical properties of CNTs (Yamabe, 1995)

Material	Young's modulus (GPa)	Tensile strength (GPa)
SWCNTs	1054	150
MWCNTs	1200	150
Diamond	600	130
Steel	208	0.4
Wood	16	0.008

Thermal properties including specific heat and thermal conductivity of carbon nanotubes are determined primarily by the phonons which are a result of lattice vibrations (Popov, 2004). The thermal conductivity of carbon nanotubes is dependent on the temperature. Especially at low temperatures, the phonon contribution to these quantities dominates (Berber, Kwon, and Tomànek, 2000). Experimental result shows thermal conductivity of SWCNTs at room temperature about 3500 $W \cdot m^{-1} \cdot K^{-1}$ (Pop et al., 2006) which compares to copper, a well-known metal for its good thermal conductivity, which transmits 385 $W \cdot m^{-1} \cdot K^{-1}$.

Theoretical and experimental results show superior electrical properties of carbon nanotubes. In theory, metallic nanotubes can produce electric current carrying capacity 1000 times higher than copper wires (Collins, and Avouris, 2000). The electronic capabilities possessed by carbon nanotubes are seen to arise predominately from interlayer interactions, rather than from interlayer interactions between multi-layers within a single carbon nanotube or between isolated nanotubes (Dresselhaus, Dresselhaus, and Saito, 1995).

Unique optical properties have proved with capabilities of acting as either a metal or semiconductor, which depend on tubule diameter and chiral angle. Metallic conduction can be achieved without introduction of doping dependence. For semi-conducting nanotubes, the band gaps have been found to be proportional to a

fraction of the diameter and without relation to the tubule chirality (Dresselhaus et al., 1995).

2.1.3 Synthesis of CNTs

There are several processes to synthesize CNTs which are difference in how carbon atoms are produced from carbon sources, including sublimation of graphite by arc discharge (Antisari, Marazzi, and Krsmanovic, 2003) and laser ablation method (Yudasaka et al., 1997) and decomposition of carbon-containing molecules by chemical vapor deposition method (Nasibulin et al., 2005).

- Arc discharge method

This method is carried out in low pressure which sealed reaction chambers and vacuum equipment are needed to provide the atmosphere. An electric arc discharge is generated between two graphite electrodes under inert atmosphere of helium or argon. A very high temperature is obtained which allows the sublimation of the carbon. Two kinds of synthesis can be performed in the arc: evaporation of pure graphite (Tang et al., 2005) or co-evaporation of graphite and metal (Liu et al., 2004). Process parameters involve small gaps between electrodes, high current, plasma between the electrodes, voltages under specified electrode dimensions.

- Laser ablation method

This is known to produce CNTs with the highest quality and high purity of single-walled CNTs (Paradise et al., 2007). In this method, a rod of graphite as carbon source and a transition metal mixture is irradiated at its surface by laser under an inert atmosphere, leading to evaporation of the mixture. Then, carbon atoms dissolve and saturate in liquid droplets of the catalyst nanoparticles at high temperature, followed by the formation of CNTs. The process parameters which affect on the formation of CNTs by laser ablation method are type and concentration of catalyst in the rod, type and power of laser, temperature and pressure of the reaction system.

- Chemical vapor deposition (CVD) method

This method involves heating carbon-containing molecules as carbon source such as acetylene (Lee et al., 2002) and ethanol (Maruyama et al., 2005) and catalyst source, including a transition metal and organometallic complex such as metallocene at high temperatures over a period of time. The carbon-containing molecules are catalytically decomposed on the catalyst nanoparticles. After that, carbon atoms diffuse and dissolve into the catalyst nanoparticles until saturation and precipitation of the carbon atoms take place to form the tubes. The characteristics of the carbon nanotubes produced by CVD method depend on the working conditions such as type of carbon and catalyst source, temperature and pressure of the system, flow rate of carrier gas and reaction time.

Mechanisms of these methods consist of diffusion, dissolution, saturation and precipitation of carbon atoms in transition metal nanoparticle acts as catalyst, in particular Fe, Co and Ni. The catalyst nanoparticles are molten to form liquid droplets where the carbon atoms can dissolve in with specific carbon solubility, depending on type of the catalyst and form into metal carbide until the carbon atoms are equilibrium in liquid-solid phase with that catalyst. As supersaturation state of carbon atoms in the catalyst, precipitation of the carbon atoms on the surface of catalyst take place, leading to the formation of the CNTs (Dupuis, 2005).

2.2 Zinc Oxide (ZnO) nanostructures

2.2.1 Structure of ZnO

ZnO is a wide band gap (3.4 eV) II-VI compound semiconductor with white powder and nearly insoluble in water but soluble in acids or alkalis. It has a stable wurtzite (hexagonal) structure with lattice constants of a = 0.325 nm and c = 0.521 nm and consists of tetrahedral coordinated zinc and oxygen atoms as shown in Figure 2.3.

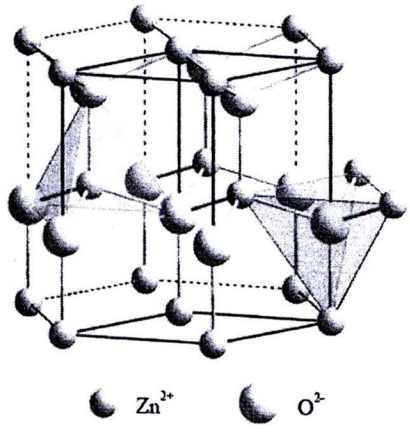

Figure 2.3 Wurtzite structure of ZnO.
http://www.thefullwiki.org/Wurtzite_(crystal_structure)

The tetrahedral coordination is also a common indicator of sp^3 covalent bonding nature. However, the Zn-O bond also possesses very strong ionic character and tends to increase the band gap beyond the one expected from the covalent bonding. Therefore, ZnO lies on the borderline between being classed as a covalent and ionic compound. Furthermore, the coordination gives rise to polar symmetry along the hexagonal axis. In such a polarity (non-centrosymmetric) structure, the center of positive charge and negative charge can be displaced due to external pressure induced lattice distortion. This displacement results in local dipole moment, thus a macroscopic dipole moment appears over the whole crystal, leading to characteristic piezoelectrical properties of ZnO.

2.2.2 Physical properties of ZnO nanostructure

The basic physical properties of bulk ZnO is shown in Table 2.3. It is worth noting that as the dimension of the semiconductor materials continuously shrinks down to nanometer or even smaller scale, some of their physical properties undergo changes known as the "quantum size effects", including mechanical, piezoelectric, electrical and optical properties.

Table 2.3 Physical properties of wurtzite ZnO (Pearton et al., 2003)

Properties	Value
Density	5.606 g/cm^3
Melting point	2248 K
Relative dielectric constant	8.66
Gap energy	3.4 eV, direct
Exciton binding energy	60 meV
Electron mobility (T = 300 K)	200 cm^2/V s
Hole mobility (T = 300 K)	5-50 cm^2/V s

ZnO is a relatively soft material with approximate hardness of 4.5 on the Mohs scale (Battez et al., 2008). Its elastic constants are smaller than those of relevant III-V semiconductors, such as GaN. The high heat capacity and heat conductivity, low thermal expansion and high melting temperature of ZnO are beneficial for ceramics (Port, 1991).

Piezoelectricity is also an important property. Among the tetrahedral bonded semiconductors, it has been stated that ZnO has a piezoelectric tensor equal to or even greater than that of GaN and AlN which means that ZnO is a suitable candidate for device applications requiring a large electromechanical coupling (Jagadish et al., 2006).

As a direct and large band-gap material, ZnO is attracting a lot of attention for a variety of electronic and optoelectronic applications. Advantages associated with a large band gap include higher breakdown voltages, ability to sustain large electric fields, lower noise generation, and high temperature and high-power operation (Özgür et al., 2005).

2.2.3 Synthesis of ZnO nanostructure

ZnO nanostructures which can be synthesized into a variety of morphologies including nanowires, nanorods, tetrapods, nanobelts, nanoflowers, nanoparticles and so on can be obtained via a variety of methods thermal evaporation, gas phase reaction and so on.

- Vapor transport synthesis process

The most common process to synthesize ZnO nanostructures utilizes a vapor transport process. In such a process, Zn vapor and oxygen source such as oxygen gas, CO and CO_2 react with each other to form ZnO nanostructures. There are several methods to generate Zn and oxygen source for the formation of ZnO nanostructures which can be categorized into following these methods.

Oxidation of Zn method, Zn powder is heated up under oxygen flow. After that, zinc vapor is oxidized to form ZnO nanostructure. Although this facilitates relative low temperature (500~700 °C), partial pressure of vaporized zinc and oxygen must be controlled carefully in order to obtain desired ZnO nanostructure. It has been observed that changing of their pressures contributes to a large variation on the morphology of nanostructure (Chang et al., 2004).

Thermal evaporation of ZnO method, decomposition of ZnO powder is direct method. However, it is limited to very high temperature (1400 °C) due to high decomposition temperature of ZnO powder (Li, Tand, and Wang, 2009).

Carbothermal reduction of ZnO method, this method is nearly the same as thermal evaporation of ZnO method. However, graphite powder as reducing agent is mixed with ZnO powder, leading to lower decomposition temperature. At about 800-1100 °C, graphite reduces ZnO to form Zn, CO and CO_2 vapors. Finally, Zn, CO and CO_2 will react to form ZnO nanostructures (Song et al., 2008).

According to the difference on nanostructure formation mechanisms, the extensively used vapor transport process can be categorized into the catalyst free vapor-solid (VS) process and catalyst assisted vapor-liquid-solid (VLS) process.

For catalyst free VS process, The Zn atoms were continuously evaporated from the source material during the heating process. In the presence of oxygen, the Zn vapors absorbed on the surface of quartz tube and react with oxygen to form ZnO nuclei. As the reactant concentration increases, the ZnO nuclei individually grow in upward direction in the form of nanostructures. In contrast, catalyst assisted VLS process; the source vapor (Zn vapor) reacted with the metal particles, which act as catalyst and from alloy droplets. After reaching at the supersaturation state, the grown droplets lead to the formation of nanostructures. The typical characteristic of VLS process is the presence of metal particles capped at the end of grown structures.

- Other synthesis processes

Although the vapor transport process is the dominant synthesis method for growing ZnO nanostructures, other growth methods such as electro-deposition and sol-gel have been developed in parallel. These methods provide the possibility of forming ZnO nanostructures at low temperature.

In an electro-deposition method (Li, Cheng, and Zhang, 2000), AAM (anodic alumina membrane) with highly ordered nanopores was used as a template. Zinc nanowires were fabricated into the nanopores via electro-deposition, forming zinc nanowires array. Then the nanowire array was oxidized at 300 °C for 2 hours and ZnO nanowire array was obtained.

In a sol-gel synthesis method (Lakshmi, Dorhout, and Martin, 1997), AAM was also used as the template and immersed into suspension containing zinc acetate for 1 minute, then heated in air at 120 °C for 6 hours. ZnO nanofibers were eventually obtained after removing the AAM template. This sol-gel process was further improved by an electrochemical method in order to obtain nanorods with diameter smaller than 50 nm.

These methods are complementary to the vapor transport synthesis of ZnO nanostructure, and also employ less rigorous synthesis conditions and provide great potential for device applications.

2.3 Composite material (Kaw, 2005)

A composite material is a structural material that consists of two or more combined constituents that are combined at a macroscopic level and are not soluble in each other. One constituent is called the reinforcing phase and the one in which it is embedded is called the matrix. The reinforcing phase material may be in the form of fibers, particles, or flakes. The matrix phase materials are generally continuous. Composites are classified by the geometry of the reinforcement or by the type of matrix as shown below.

- *Particulate composites* consist of particles immersed in matrices such as alloys and ceramics. They are usually isotropic because the particles are added randomly. Particulate composites have advantages such as improved strength,

increased operating temperature, oxidation resistance and so on. Typical examples include use of aluminum particles in rubber, silicon carbide particles in aluminum and gravel, sand and cement to make concrete.

- *Flake composites* consist of flat reinforcements of matrices. Typical flake materials are glass, mica, aluminum, and silver. Flake composites provide advantages such as high out-of-plane flexural modulus, higher strength, and low cost. However, flakes can not be oriented easily and only a limited number of materials are available for use.

- *Fiber composites* consist of matrices reinforced by short (discontinuous) or long (continuous) fibers. Fibers are generally anisotropic and examples include carbon and aramids. Examples of matrices are resins such as epoxy, metals such as aluminum, and ceramics such as calcium-alumino silicate.

- *Nanocomposites* consist of materials that are of the scale of nanometers. The accepted range to be classified as a nanocomposite is that one of the constituents is less than 100 nm. At this scale, the properties of materials are different from those of the bulk material. Generally, advanced composite materials have constituents on the microscale. By having materials at the nanometer scale, most of the properties of the resulting composite material are better than the ones at the microscale. Not all properties of nanocomposites are better, in some cases, toughness and impact strength can decrease.

2.4 Differential Mobility Analyzer (DMA)

Depending on the location where nucleation and growth of the synthesized nanoparticles by gas phase reaction take place, these synthesis processes can be divided into two categories; (i) supported nanoparticles on substrates and (ii) floating nanoparticle synthesis process. In the supported nanoparticle synthesis process, the synthesized nanoparticles are supported on a substrate such as single-walled carbon nanotubes (SWCNTs) can be produced by the supported catalyst process such as the supergrowth technique (Futaba et al., 2005). Conversely, in the floating nanoparticle synthesis process usually referred to as aerosol synthesis process,

the synthesized nanoparticles are suspended in the gas stream through out the formation.

In case of the floating nanoparticle synthesis process, an important physical parameter for characterizing the behavior of these particles is the size. It is therefore desirable to measure and classify the size of the particles and to yield monodisperse particles to gain understanding of the particle dynamics and control particle contamination. Among the various methods developed for the analysis of nanometer aerosol particles, differential mobility analyzer (DMA) has become the most common instrument widely used for classifying and generating monodisperse particles such as combination of laser ablation and electrostatic classification could provide a narrow size range of multi-walled carbon nanotubes (MWCNTs) and generated monodisperse MWCNTs from acetylene/hydrogen mixture using the monodisperse nickel nanoparticles (Kim and Zachariah, 2007).

A typical setup of a general DMA shown in Figure 2.4 consists of two concentric metal electrodes with the inner electrode maintained at a controlled negative voltage, in range of 1 V and 10 kV, while the outer electrode is electrically grounded, leading to creation of an electric field between these electrodes.

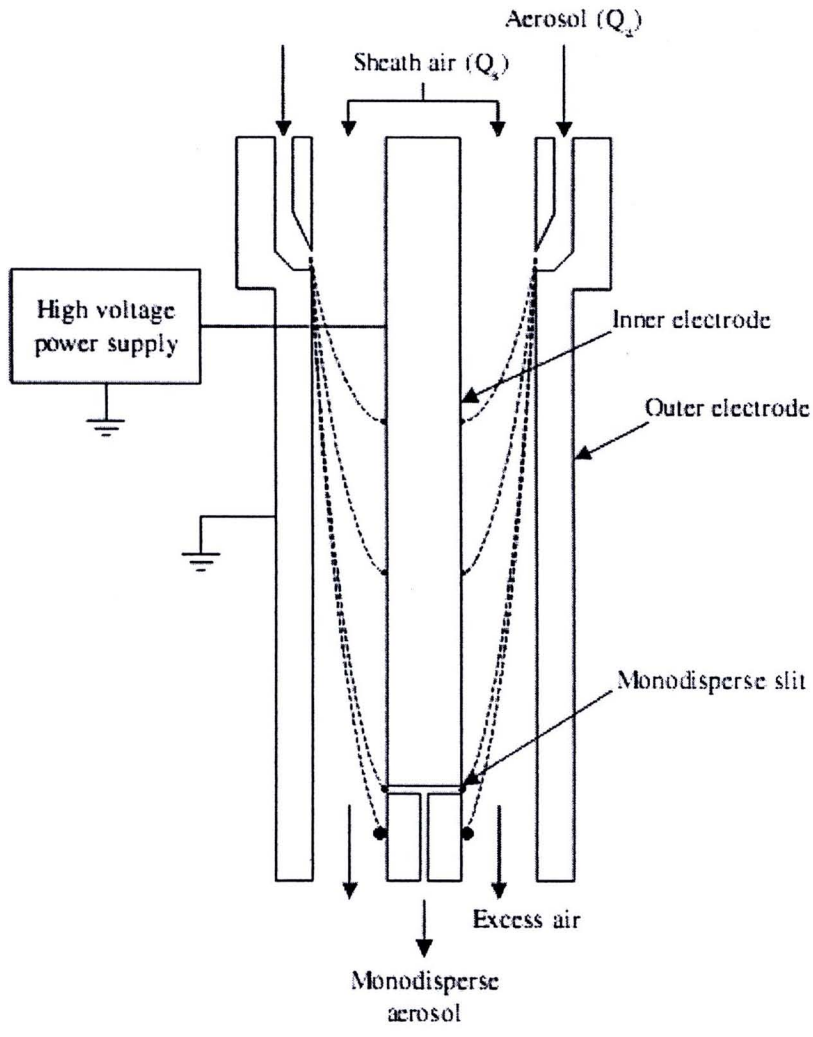

Figure 2.4 Differential Mobility Analyzer (DMA) for classifying and generating monodisperse aerosol particles (Intra, and Tippayawong, 2008)

The polydisperse charged aerosol (Q_a) and particle-free sheath air (Q_s) are introduced at the top of the DMA and flow down the annular space between the electrodes. The aerosol surrounds the inner core of sheath air, and both flows pass down the annulus with no mixing of the two laminar streams. The electric field causes positively charged particles to be attracted through the sheath air to the negative charged inner rod. Particles are collected along the length of the inner rod. The location of the collecting particles depends on the particle electrical mobility (Z_p), the fluid flow rate, and the DMA geometry. The electrical mobility of the collected particles is a function of the dimensions of the DMA, the applied voltage, and the fluid flow rate as shown in equation 2.2 proposed by Knutson, and Whitby (1975).

$$Z_p = \frac{(Q_s + Q_a)\ln(R_2 / R_1)}{2\pi LV} \tag{2.2}$$

where

Z_p = Electrical mobility of the collected particles

R_1 = Radius of the inner electrode

R_2 = Radius of the outer electrode

L = Length of electrode

V = Applied voltage

From Stokes' law, the electrical mobility is related to particle diameter (d_p) as shown in equation 2.3

$$d_p = \frac{neC_c}{3\pi\mu Z_p} \tag{2.3}$$

where

n = Number of elementary charge units

e = Elementary unit of charge (1.61×10^{-19} C)

C_c = Cunningham slip correction factor

μ = Gas viscosity

The Cunningham slip correction factor is a function of the particle Knudsen number (K_n) proposed by Cunningham, 1910 shown in equation 2.4.

$$C_c = 1 + K_n\left[1.257 + 0.4\exp(-1.1/K_n)\right] \tag{2.4}$$

where

$$K_n = \frac{2\lambda}{d_p}$$

Particles with a high electrical mobility are collected along the upper portion of the rod. Particles with a low electrical mobility are collected on the lower portion of the rod. Particles with narrow range of electrical mobility exit with the monodisperse air flow through a small slit located at the bottom of the inner rod.

These particles are transferred to a particle counter to determine the particle number concentration such as condensation particle counter (CPC). The remaining particles are exhausted out as excess air flow. The size distribution is obtained by varying the applied voltage.

2.5 Gibbs free energy of reaction (Gaskell, 1981)

The Gibbs free energy (ΔG) of a reaction is a measure of the thermodynamic driving force that makes a reaction occurs. A negative value for ΔG indicates that a reaction can proceed spontaneously without external inputs, while a positive value indicates that it will not. The equation for Gibbs free energy of the reaction is shown in equation 2.5.

$$\Delta G = \Delta H - T\Delta S \tag{2.5}$$

where ΔH = Enthalpy of the reaction
ΔS = Entropy of the reaction
T = Temperature of the reaction

The enthalpy (ΔH) is a measure of the actual energy that is liberated when the reaction occurs (the heat of reaction). If it is negative, then the reaction gives off energy (exothermic reaction), while if it is positive the reaction requires energy (endothermic reaction). The entropy (ΔS) is a measure of the change in the possibilities for disorder in the products compared to the reactants. For example, if a solid (an ordered state) reacts with a liquid (a somewhat less ordered state) to form a gas (a highly disordered state), there is normally a large positive change in the entropy for the reaction.

2.6 Reaction equilibrium in a system containing condensed phases and a gaseous phase (Gaskell, 1981)

Consider the reaction equilibrium between a pure solid metal M, its pure oxide MO and O_2 at the temperature T and the pressure P as shown in equation 2.6.

$$M(s) + \frac{1}{2} O_2(g) = MO(s) \qquad (2.6)$$

It is considered that O_2 is insoluble in the solid metal. Both the metal M and the oxide MO exist as vapor species in the gas phase, as is required by the criteria for phase equilibria,

$$\bar{G}_M \text{ (in the gas phase)} = G_M \text{ (in the solid metal phase)} \qquad (2.7)$$

$$\bar{G}_{MO} \text{ (in the gas phase)} = G_{MO} \text{ (in the solid metal phase)} \qquad (2.8)$$

Therefore, reaction equilibrium is established in the gas phase. The equilibrium of interest is thus

$$M(g) + \frac{1}{2} O_2(g) = MO(g) \qquad (2.9)$$

The free energy of the reaction can be written as in equation 2.10

$$G^{\circ}_{MO(g)} - \frac{1}{2} G^{\circ}_{O_2(g)} - G^{\circ}_{M(g)} = -RT \ln \frac{p_{MO}}{p_M \, p_{O_2}^{\frac{1}{2}}} \qquad (2.10)$$

or

$$\Delta G^{\circ} = -RT \ln \frac{p_{MO}}{p_M \, p_{O_2}^{\frac{1}{2}}}$$

where ΔG° = Difference between the free energy of 1 mole of gaseous MO at 1 atm pressure, and the sum of the free energies of a half of 1 mole of O_2 at 1 atm pressure and 1 mole of gaseous M at 1 atm pressure, all at the temperature T

p_{MO} = Equilibrium vapor pressure of solid MO at the temperature of T

p_M = Equilibrium vapor pressure of solid M at the temperature of T

p_{O_2} = Equilibrium pressure of O_2 at the temperature of T

Equation 2.7 and 2.8 can be written as equation 2.11 and 2.12, respectively.

$$G^{\circ}_{M(g)} + RT \ln p_{M(g)} = G^{\circ}_{M(s)} + \int_{P=1}^{P=p_{M(g)}} V_{M(s)} dP \qquad (2.11)$$

$$G^{\circ}_{MO(g)} + RT \ln p_{MO(g)} = G^{\circ}_{MO(s)} + \int_{P=1}^{P=p_{MO(g)}} V_{MO(s)} dP \qquad (2.12)$$

where $G^{\circ}_{M(g)}$ = Molar free energy of the gaseous M under a pressure of 1 atm and the temperature T

$G^{\circ}_{M(s)}$ = Molar free energy of the solid M under a pressure of 1 atm and the temperature T

$G^{\circ}_{MO(g)}$ = Molar free energy of the gaseous MO under a pressure of 1 atm and the temperature T

$G^{\circ}_{MO(s)}$ = Molar free energy of the solid MO under a pressure of 1 atm and the temperature T

$V_{M(s)}$ = Molar volume of the solid M at the pressure of P and the temperature of T

$V_{MO(s)}$ = Molar volume of the solid MO at the pressure of P and the temperature of T

It is to be noted that the value of the integral terms of $\int_{P=1}^{P=p_{M(g)}} V_{M(s)} dP$ and $\int_{P=1}^{P=p_{MO(g)}} V_{MO(s)} dP$ are small enough to be considered negligible. Therefore, equation 2.11 and 2.12 can be reduced into equation 2.13 and 2.14, respectively.

$$G^{\circ}_{M(g)} + RT \ln p_{M(g)} = G^{\circ}_{M(s)} \qquad (2.13)$$

$$G^{\circ}_{MO(g)} + RT \ln p_{MO(g)} = G^{\circ}_{MO(s)} \qquad (2.14)$$

Equation 2.10 can be written as shown in equation 2.15

$$G^{\circ}_{MO(s)} - \frac{1}{2} G^{\circ}_{O_2(g)} - G^{\circ}_{M(s)} = -RT \ln \frac{1}{p^{\frac{1}{2}}_{O_2}} \qquad (2.15)$$

or

$$\Delta G^{\circ} = -RT \ln K$$

where ΔG° = Standard free energy of reaction $M(s) + \frac{1}{2} O_2(g) = MO(s)$

$$K = \frac{1}{p^{\frac{1}{2}}_{O_2}}$$

Thus in the case of reaction equilibria involving pure condensed phase and a gas phase, the equilibrium constant K can be written solely in terms of those species which occur only in the gas phase. ΔG° is a function only of temperature, then K is a function of temperature, and hence at any fixed temperature the establishment of reaction equilibrium occurs at a unique value of $p_{O_2} = p_{O_2(eq,T)}$.

If, at any temperature, T, the actual O_2 partial pressure in a closed metal-metal oxide-oxygen system is greater than $p_{O_2(eq,T)}$, then spontaneous oxidation of the metal will occur, thus consuming O_2 and decreasing the O_2 pressure in the gas phase. When the actual O_2 partial pressure has thus been lowered to $p_{O_2(eq,T)}$, then, provided that both solid phases are still present, the oxidation reaction ceases and equilibrium prevails. Similarly, if the O_2 partial pressure in a closed metal-metal oxide-oxygen system was originally less than $p_{O_2(eq,T)}$, then spontaneous reduction of the oxide would occur until $p_{O_2(eq,T)}$ was reached.

2.7 Ellingham diagram for oxides

Ellingham (1944) plotted the experimentally determined ΔG°-T relationships for the oxidation of a series of metals. The general forms of the relationships approximated to straight lines over temperature ranges. The relations could thus be expressed by means of the simple equation as shown in equation 2.16

$$\Delta G^{\circ} = A + BT \qquad (2.16)$$

where A = Temperature-independent standard enthalpy change, ΔH°

B = Negative of temperature-independent standard entropy change, $-\Delta S^{\circ}$

The variation of ΔG° with T at constant total pressure is plotted for oxidation reactions of various metals such as Fe, Ni, Cr and Zn is known as an Ellingham diagram shown in Figure 2.5.

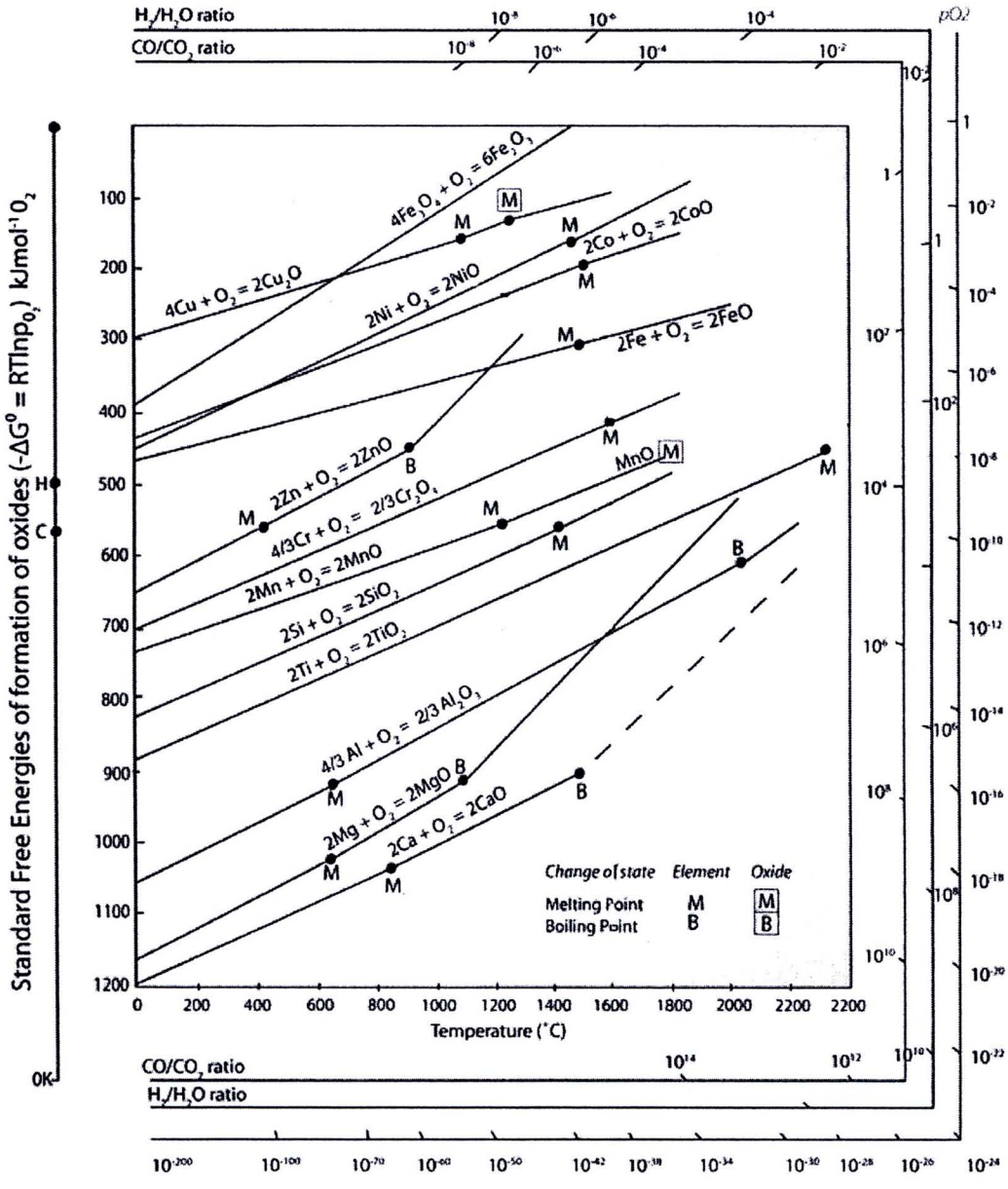

Figure 2.5 Ellingham diagram for metallurgical oxides.
(http://www.doitpoms.ac.uk/tlplib/ellingham_diagrams/ellingham.php)

From equation 2.16, ΔH° is the intercept of the line with the T = 0 K axis, and ΔS° is the negative of the slope of the line. As ΔS° is a negative quantity, the line has a positive slope. The value of ΔG° for an oxidation reaction is thus a measure of the chemical affinity of the metal for O_2, and the more negative the value of ΔG° at any temperature, then the more stable the oxide.

2.8 Literature Reviews

2.8.1 Investigation of synthesis of the SWCNTs by laser ablation

Yudasaka et al. (1999) studied the formation of the SWCNTs by the Nd:YAG laser ablation of 3 different targets, including C/Ni/Co, C/Ni and C/Co. The target was placed at the center of a quartz tube reactor and then heated up to 1197 °C. The Nd:YAG laser beam (wavelength of 532 nm, pulse width of 6-7 ns and frequency of 10 Hz) irradiated the target surface perpendicularly for 60 s under Ar flow. The results exhibited the yield of SWCNTs on the target composition with yields following the order C/Ni/Co > C/Ni >> C/Co. The SWCNT bundles formed when using target of C/Ni/Co is thicker and longer than those of C/Ni. The diameters of the SWCNTs when using C/Ni/Co target were larger and more uniform than those of C/Ni.

Yudasaka et al. (1997) synthesized SWCNTs by pulsed Nd:YAG laser ablation of C/Ni/Co target. The effects of the power of laser and the target composition on the formation of the SWCNTs were investigated. The target was heated up to 1200 °C under the optimum pressure and flow rate of 500-600 Torr and 0.2-0.5 L/min, respectively. The Nd:YAG laser beam (wavelength of 532 nm, pulse width of 7 ns, frequency of 10 Hz and power of 1.2 J/pulse) irradiated the target surface perpendicularly. The SWCNTs were formed when the power of the laser in a range of 1.1-4.4 W. However, the power was larger than 5.4 W, the quantity of the SWCNTs decreased dramatically. Decreasing of Ni and Co in the target composition provided increasing of the SWCNT yield with higher laser power.

Kataura et al. (2000) investigated the effect of furnace temperature on the formation of the SWCNTs by laser ablation of C/Ni/Co target. The target with Ni/Co of 0.45/0.45 at.% was inserted into the quartz tube reactor and then heated up in a range of 800-1350 °C under 500 Torr of Ar. After that, the Nd:YAG laser irradiated the target surface perpendicularly. At the furnace temperature of 800 °C, the SWCNTs with a very small diameter were synthesized, but the abundance was very low. When the furnace temperature was increased, the SWCNTs were synthesized with high abundance and purity.

Detail of proposed reviews of the synthesis of the SWCNTs by Nd:YAG pulse laser ablation is summarized in Table 2.4.

2.8.2 Investigation of synthesis of the carbon nanoparticles by CVD

Charinpanitkul et al. (2009) studied synthesis of the carbon nanoparticles by CVD of naphthalene and ferrocene. A mixture of naphthalene and ferrocene with a constant ratio of 1:1 was loaded into a graphite boat and then inserted into a quartz tube reactor where the local temperature was kept above the vaporization temperature of the mixture. The reaction temperature was varied in a range of 800-1050°C. The synthesized products were combination of carbon nanocapsules (CNCS) and MWCNTs. The increasing of temperature resulted in the enhance formation of CNCs with lower amount of the CNTs. The experimental results also revealed that the total yield of the products could be enhanced with the increased reaction temperature.

Musso et al. (2008) synthesized CNTs using CVD of camphor and ferrocene. The effect of temperature on the formation of the CNTs on crystalline silicon substrate was investigated. A mixture of camphor and ferrocene with a 20/1 mass ratio was prepared in a flask which connected to the quartz tube reactor. The substrate was inserted into a quartz tube reactor and then heat up in a range of 800-1000 °C. Subsequently, the flask was heated up to 220 °C, leading to the vaporization of the mixture, and the vaporized mixture were carried into the reactor by the flow of nitrogen. At a substrate temperature in the range of 650-900 °C, a carpet of vertically oriented CNTs, with spare signs of other forms of carbon, was obtained on silicon substrate. On the other hand, the film grown on the silicon substrate in the temperature range of 950-1070 °C showed the formation of a nanographite layer and carbon fibers.

Andrews et al. (1999) studied the formation of the MWCNTs by CVD of ferrocene-xylene mixture. The mixture of ferrocene and xylene was fed into a two-stage tubular quartz reactor using syringe pump. The liquid feed was then preheated to 175 °C. At this temperature, the liquid was immediately vaporized and swept into the reaction zone of the furnace by flow of Ar. Various parameters, such as the furnace temperature (650-1050 °C), ferrocene/xylene ratio and feed rate, total reaction time

and gas flow rate, were adjusted to determine the growth conditions for high purity aligned MWCNTs.

The results revealed that at 1050 °C, a small amount of the MWCNTs was formed at the entrance of the furnace. However, when the reactor temperature was lowered to 675 °C, copious amounts of aligned MWCNTs were produced. At a xylene partial pressure of 4 mbar, the MWCNTs were found only. However, at a higher xylene partial pressure of 20 mbar, amorphous carbons were observed only. At a Fe/C ratio of 0.75 at.% showed the presence of the Fe catalyst inside the core of the MWCNTs. Lowering the Fe/C ratio by a factor of 10 produced longer and thinner nanotubes and the Fe catalyst was absent inside the core of the tubes.

Detail of proposed reviews of the synthesis of the MWCNTs by CVD under atmospheric pressure is summarized in Table 2.5.

2.8.3 Investigation of synthesis of the ZnO nanoparticles by oxidation

Park et al. (2006) studied the growth of ZnO nanowires using few amount of oxygen. The ZnO nanowire has grown from metal Zn granule under controlled O_2 environments. The effects of oxygen concentration and temperature on the formation of the ZnO nanowires were investigated. The total flow rate of oxygen and nitrogen was controlled at 200 mL/min, while the oxygen concentration was adjusted from 0.5 to 5 vol%. The temperature was varied in a range of 700-1000 °C. The ZnO nanowires became shorter when oxygen concentration was increased. ZnO nanorods became nanowires and needles when the temperature was varied from 700 to 800 and 900 °C, respectively.

Umar et al. (2005) studied formation of ZnO nanorods with large quantity using metallic zinc powder and oxygen. A quartz boat of Zn was inserted into a quartz tube reactor and then heated up to the temperature ranges of 500-620 °C under pressure of 3 Torr. Nitrogen and Oxygen flow rates were introduced into the system with their flow rates of 10 and 20 sccm, respectively. General morphologically studies indicated the as-grown products are flower-shaped containing several hundreds of nanorods. The obtained nanorods have a diameter of 150-250 nm while

their lengths are 5-10 μm. The detailed structural analysis revealed that the ZnO nanorods exhibit a single crystalline wurtzite phase containing very less structural defects.

Dai et al. (2002) synthesized tetrapod ZnO nanoparticles using oxidation reaction between pure Zn and oxygen. Alumina boat which loaded Zn was inserted in a horizontal tube furnace. The temperature of furnace was ramped to 825-925 °C at heating rate of 50-100 °C/min. From FE-SEM images, ZnO nanoparticles were a tetrapod shape having four legs with diameter 70-150 nm and length of legs was 2-3 μm. In detailed structure of individual ZnO was characterized by using TEM. From bright-field images, there was no streaking in the nanorod. From dark-field images, single crystal nature of nanorod was observed. Therefore, ZnO nanoparticles which use oxidations in gas phase were high-quality nanocrystal.

Wu and Xie (2004) studied about synthesis of ZnO nanoparticles using the oxidation reaction between Zinc vapor and oxygen at various temperatures (1050-1400 °C) and pressure (1-12 kPa). The powder Zn was vaporized by using inductive furnace. Firstly, Zn vapor contacted with argon atoms in the gas mixture because the molecular weight of argon atom is heavier than oxygen atom. Then, Zn vapor was condensed to Zn aerosol. In the same time, Zn aerosol reacted with oxygen atom to produced ZnO nanoparticles.

As-synthesis ZnO have four needle-like feet (tetrapod) with diameter of 6-45 nm and length 280-435 nm. While the temperature was raised, the diameter of ZnO increased and the length of ZnO decreased. The ZnO nanoparticles of different sizes were obtained in range of gas pressure at each evaporation temperature. For example at 1350 °C, the pressure was varied from 2.2 to 6 kPa and the nanowhiskers with longest needle-like feet were obtained at a pressure of 4 kPa. However, the spheroid nanoparticles were obtained out side this pressure range.

Detail of proposed reviews of the synthesis of the ZnO nanoparticles by oxidation is summarized in Table 2.6.

2.8.4 Investigation of synthesis of the ZnO/MWCNT composites

Chrissanthopoulos et al. (2007) reported synthesis of various ZnO nanostructures grown on multi-walled carbon nanotubes by thermal evaporation method. The influence of deposition time at 4, 8 and 15 min and substrate temperature at 850-900 °C were investigated. An equimolar zinc oxide and graphite was mixed and then put on boat placed at the closed end of a fused silica tube. The MWCNTs were used as received. The mixture was inserted for few minutes in a preheated (at ~1000 °C) horizontal furnace, while the CNTs pellets were placed at various position at a temperature interval 850-950 °C.

The experiment showed various structures such as polypods and nano-hedgehogs, depending on various factors as well as the location of the ZnO–CNT junction. Single, isolated nanorods appear to form at the end of a CNT.

Chen et al. (2006) presented zinc oxide nanoparticles decorated multi-walled carbon nanotubes. MWCNTs were prepared by the chemical catalytic vapor deposition process (CVD) of acetylene. The obtained MWCNTs were modified with citric acid, which were sonicated 30 min and refluxed at 80 °C. Then, the mixture was filtered, washed and dried at 60 °C. The ZnO/MWCNTs composites were prepared using a sol-gel method, in which zinc acetate was dissolved in anhydrous ethanol. Finally, the modified MWCNTs were added. The additions were accompanied by stirring and sonication. The temperature was maintained at 60 °C. Finally, the ZnO/MWCNTs precursor was dried at 70 °C and then calcined at 450, 600 and 750 °C, respectively for 2 h under the protection of nitrogen.

The results reveal that the MWNT are decorated with ZnO particles. The average size of calcined ZnO at 450, 600 and 750 °C was about 11, 48 and 89 nm, respectively. Furthermore, the UV emission of MWCNTs was improved significantly through modification with ZnO.

Du, Hao, and Wang (2008) presented the preparation of floral-patterned ZnO/MWCNTs heterogeneity structure by using microwave irradiation heating method. Pristine nanotubes were refluxed in nitric acid at 140 °C for 4 h. Then, zinc acetate was added into the MWCNTs solution. The solution was placed in

a microwave oven with an outside refluxing system and irradiated for 2 min. Finally, the suspension was washed with ethanol and deionized water by centrifugation, then dried at 60 °C under air atmosphere.

It was found that the flower-like zinc oxide grows around the multi-walled carbon nanotubes to form a floral-patterned structure. Multi-walled carbon nanotubes play a role as a template for the growth of ZnO and they can link ZnO particles together as a complex fabrication. The flower-like zinc oxide is uniform and has an average diameter of 2 micron. The average length of flower petals is about 1 micron.

Jiang, and Gao (2005) studied the fabrication and characterization of ZnO-coated multi-walled carbon nanotubes with photocatalytic activity. MWCNTs were prepared by the catalytic decomposition of methane. The pristine nanotubes were dispersed in a dilute sodium dodecyl sulfate (SDS) aqueous solution by using the ultrasonication. ZnO nanoparticles were achieved via the reaction of zinc acetate and lithium hydroxide monohydrate in a hydrous ethanol medium. Ethanol solution containing Zn^{2+} and SDS-coated MWCNTs were refluxed at 80 °C for 3 h. Then, the mixture was boiled at 95 °C for 3 h. The final black product was rinsed repeatedly with ethanol and distilled water, and then vacuum dried at 60 °C for 12 h.

It can be observed that most of MWCNTs containing individual CNTs and CNT bundles have been covered with ZnO nanoparticle layers with an average size of ~6 nm. The composite shows enhanced photocatalytic degradation of methylene blue solution.

Detail of proposed reviews of the synthesis of the composite of ZnO and MWCNTs is summarized in Table 2.7.

Table 2.4 Literature reviews of the synthesis of the SWCNTs by Nd:YAG pulse laser ablation

Researcher	Target type	Target composition	Laser intensity	Ar flow rate	Temperature	Pressure	Experimental results
Yudasaka et al. (1999)	C/Ni/Co	0.0-4.5 % atom each of Ni and Co	1-6 W	0.5 L/min	1197 °C	600 Torr	SWCNTs with yields following the order C/Ni/Co > C/Ni >>C/Co
	C/Ni	0.15-0.9 % atom of Ni					
	C/Co	0.6-9.0 % atom of Co					
Yudasaka et al. (1997)	C/Ni/Co	0.6-4.5 % atom each of Ni and Co	1.1-9.1 W	0.2-0.5 L/min	1200 °C	500-600 Torr	SWCNTs at the laser intensity lower than 4.4 W
Kataura et al. (2000)	C/Ni/Co	0.45 % atom each of Ni and Co		1.2-12 mm/s	800-1350 °C	500 Torr	Change in diameter distribution of SWCNTs at changing flow velocity

Table 2.5 Literature reviews of the synthesis of the MWCNTs by CVD under atmospheric pressure

Researcher	Carbon precursor	Catalyst precursor	Carbon/Catalyst molar ratio	Carrier gas flow rate	Temperature		Deposition time	Experimental results
					Preheater	Reactor		
Charinpanitkul et al. (2009)	Naphthalene	Ferrocene	20/1	N_2 rate of 0.12 L/min	-	800-1050 °C	15 min	MWCNTs and Carbon naocapsules (CNCs)
Musso et al. (2008)	Camphor	Ferrocene	24/1	N_2 rate of 0.42 L/min	220 °C	800-1100 °C	20 min	Vertically aligned MWCNTs
Andrews et al. (1999)	Xylene	Ferrocene	15/1 with feed rate of 1-5 mL/h	Ar + 0.1 % H_2 with total rate of 0.75-1.88 L/min	175 °C	650-1050 °C	120 min	Aligned MWCNTs

Table 2.6 Literature reviews of the synthesis of the ZnO nanoparticles by oxidation of Zn

Researcher	O_2 flow rate	Carrier gas flow rate	Temperature)	Pressure	Reaction time	Experimental results
Park et al. (2006)	1-10 mL/min	190-199 mL/min	700-1000 °C	760 Torr		ZnO nanowire, nanorod, nanoneedle
Umar et al. (2005)	20 mL/min	N_2 rate of 10 mL/min	500-620 °C	3 Torr	60-90 min	Flower-shaped ZnO containing several hundreds of nanorods
Dai et al. (2002)			825-925 °C	760 Torr	1-30 min	ZnO tetrapod
Wu et al. (2004)	25 mL/min	Ar rate of 25 mL/min	1050-1400 °C	7.5-90 Torr	15 min	ZnO nanowhisker

Table 2.7 Literature reviews of the synthesis of the ZnO/MWCNT composite

Researcher	CNTs			Fabrication of ZnO on the CNTs		Experimental results
	Method	Synthesizing temperature	N_2 flow rate	Method	Synthesizing temperature	
Chrissanthopoulos et al. (2007)	Commercial grade	-	-	Carbothermal reduction of ZnO	1000 °C	Single, isolated ZnO nanorod on the end of a MWCNT.
Chen et al. (2006)	CVD of acetylene	700 °C	0.24 L/min	Sol-gel of zinc acetate	60 °C	MWCNT decorated with ZnO particles
Du et al. (2008)	Commercial grade	-	-	Sol-gel of zinc acetate		Flower-like ZnO grown around the multi-walled carbon nanotubes
Jiang et al. (2005)	Commercial grade	-	-	Sol-gel of zinc acetate	80 °C	MWCNTs covered with ZnO nanoparticle